



Article

Using CYGNSS Data to Map Flood Inundation during the 2021 Extreme Precipitation in Henan Province, China

Shuangcheng Zhang^{1,2}, Zhongmin Ma^{1,*}, Zhenhong Li^{1,3,4} , Pengfei Zhang⁵, Qi Liu^{1,6}, Yang Nan⁷, Jingjiang Zhang⁸, Shengwei Hu¹, Yuxuan Feng¹ and Hebin Zhao¹

- ¹ College of Geology Engineering, Chang'an University, Xi'an 710054, China; shuangcheng369@chd.edu.cn (S.Z.); zhenhong.li@chd.edu.cn (Z.L.); liuqi.vip@chd.edu.cn (Q.L.); 2020126014@chd.edu.cn (S.H.); 2020226016@chd.edu.cn (Y.F.); 2021226071@chd.edu.cn (H.Z.)
- ² State Key Laboratory of Geo-Information Engineering, Xi'an 710054, China
- ³ Big Data Center for Geosciences and Satellites, Chang'an University, Xi'an 710054, China
- ⁴ Key Laboratory of Western China's Mineral Resources and Geological Engineering, Ministry of Education, Xi'an 710054, China
- ⁵ National Time Service Center, Chinese Academy of Sciences, Xi'an 710600, China; zhangpengfei@ntsc.ac.cn
- ⁶ Earth Observation Research Group, Institute of Space Sciences (ICE, CSIC), 08290 Barcelona, Spain
- ⁷ GNSS Research Center, Wuhan University, Wuhan 430079, China; nanyang@whu.edu.cn
- ⁸ Institute of Urban Meteorology, China Meteorological Administration, Beijing 100089, China; jjzhang@ium.cn
- * Correspondence: zhongminma@chd.edu.cn



Citation: Zhang, S.; Ma, Z.; Li, Z.; Zhang, P.; Liu, Q.; Nan, Y.; Zhang, J.; Hu, S.; Feng, Y.; Zhao, H. Using CYGNSS Data to Map Flood Inundation during the 2021 Extreme Precipitation in Henan Province, China. *Remote Sens.* **2021**, *13*, 5181. <https://doi.org/10.3390/rs13245181>

Academic Editors: Kegen Yu, Joon Wayn Cheong and Sajad Tabibi

Received: 28 November 2021
Accepted: 16 December 2021
Published: 20 December 2021

Publisher's Note: MDPI stays neutral with regard to jurisdictional claims in published maps and institutional affiliations.



Copyright: © 2021 by the authors. Licensee MDPI, Basel, Switzerland. This article is an open access article distributed under the terms and conditions of the Creative Commons Attribution (CC BY) license (<https://creativecommons.org/licenses/by/4.0/>).

Abstract: On 20 July 2021, parts of China's Henan Province received the highest precipitation levels ever recorded in the region. Floods caused by heavy rainfall resulted in hundreds of casualties and tens of billions of dollars' worth of property loss. Due to the highly dynamic nature of flood disasters, rapid and timely spatial monitoring is conducive for early disaster prevention, mid-term disaster relief, and post-disaster reconstruction. However, existing remote sensing satellites cannot provide high-resolution flood monitoring results. Seeing as spaceborne global navigation satellite system-reflectometry (GNSS-R) can observe the Earth's surface with high temporal and spatial resolutions, it is expected to provide a new solution to the problem of flood hazards. Here, using the Cyclone Global Navigation Satellite System (CYGNSS) L1 data, we first counted various signal-to-noise ratios and the corresponding reflectivity to surface features in Henan Province. Subsequently, we analyzed changes in the delay-Doppler map of CYGNSS when the observed area was submerged and not submerged. Finally, we determined the submerged area affected by extreme precipitation using the threshold detection method. The results demonstrated that the flood range retrieved by CYGNSS agreed with that retrieved by the Soil Moisture Active Passive (SMAP) mission and the precipitation data retrieved and measured by the Global Precipitation Measurement mission and meteorological stations. Compared with the SMAP results, those obtained by CYGNSS have a higher spatial resolution and can monitor changes in the areas affected by the floods over a shorter period.

Keywords: Cyclone Global Navigation Satellite System; flood inundation; extreme precipitation; global navigation satellite system-reflectometry; Soil Moisture Active Passive

1. Introduction

Henan Province, a provincial-level administrative region of China, is located in central China (31°23'–36°22' N, 110°21'–116°39' E). The terrain is high in the west; low in the east; and composed of plains, basins, mountains, and hills. It crosses four river basins, namely the Haihe River, Yellow River, Huaihe River, and Yangtze River, and average annual rainfall in the region is 500–900 mm [1]. In mid-to-late July 2021, the central and northern parts of Henan Province were hit by extreme precipitation. Floods and other secondary disasters caused by heavy rainfall have greatly endangered the property and safety of local residents [2,3].

Timely and accurate mapping of the scope of the submerged area affected by a flood can provide rescue personnel critical information for decision making. Additionally, this mapping can improve the understanding of the temporal and spatial characteristics of floods over time to support flood forecasting and early-warning methods [4–6]. Satellite remote sensing is considered an effective method for monitoring flood disasters [7]. However, the ground surface is usually covered by thick clouds during floods; therefore, optical remote sensing is limited [8]. Microwave remote sensing is not typically affected by clouds or vegetation. Many researchers report that this sensing method is the best means of monitoring flood disasters [9,10]. However, the spatial or temporal resolution of the data provided by existing microwave remote sensing satellites is limited [11].

Global Navigation Satellite System-Reflectometry (GNSS-R) is an emerging remote sensing technology based on the reflected signals of navigation satellites. As early as 1988, Hall and Cordey proposed the idea of using Global Positioning System (GPS) scattered signals to sense the roughness of the sea surface [12]. Moreover, in 1993, Martin-Neira of the European Space Agency proposed the Passive Reflection and Interferometry System, which uses passive reflection and interferometry technology for remote ocean sensing [13]. Subsequently, Zavorotny and Voronovich suggested a scientific model based on the Kirchhoff approximation and geometric optics limit (Z-V model) in 2000, which explained GPS signals scattered by the ocean and laid the theoretical foundation of this new technology [14]. Since then, theoretical studies and experiments worldwide have been carried out on GNSS reflected signals, including the development of new GNSS-R receivers; altimeter and scatterometer tests based on different platforms such as shore-based, tower-based, airplane, etc.; and research on signal reception, principle verification, and the feasibility of using GNSS-R to estimate ocean parameters (sea surface height, sea surface wind, sea surface roughness, etc.). GNSS-R remote sensing apparatuses have gradually shifted from ground and airplane platforms to satellite platforms, and the research objectives have extended beyond oceans to land, atmosphere, and polar regions [15–20]. In recent years, the successful launches of many GNSS-R low-orbit satellites have opened a new era for spaceborne GNSS-R. The first satellite-borne on-orbit verification research was carried out by the American Jet Propulsion Laboratory using the satellite-borne imaging radar-C mounted on the space shuttle [21], which promoted the development of satellite-based GNSS-R. Subsequently, many satellites, including Britain's Disaster Monitoring System-1 [22] and Britain's Techdemosat-1 [23], have implemented many GNSS-R on-board studies.

The Cyclone Global Navigation Satellite System (CYGNSS) is a GNSS-R LEO satellite formation consisting of eight small satellites launched by NASA at the end of 2016, with an orbital height of approximately 524 km. Each small satellite is equipped with a special four-channel GNSS-R payload for transmitting reflected signals in the L1 band of the GPS, and the observation range is approximately 38 south latitude to 38 north latitude [24–26]. Although the application of CYGNSS in monitoring sea surface wind has been used for some time [26–28], its data have been proven to invert many land parameters, such as soil moisture [29–32], biomass [33], wetland monitoring [34,35], inland water bodies [36–38], and target detection [39] with increasing research. The feasibility of using CYGNSS data to monitor floods was first confirmed by Chew et al. [40] through the successful use of CYGNSS data to map the flood inundation in the southeastern United States and the Caribbean during the 2017 Atlantic hurricane season. The results show that compared to SMAP brightness temperature data and Landsat optical images, the results obtained by CYGNSS have higher temporal and spatial resolutions. Wei Wan et al. [41] utilized CYGNSS data to map the distribution of inundated areas affected by heavy rainfall during the 2017 Chinese typhoon season. Studies have shown that the results of the flooding area distribution obtained by CYGNSS are in good agreement with rainfall data, SMAP, and SMOS brightness temperature data. Rajabi et al. [42] studied the feasibility of using CYGNSS data to detect and map flood distributions during heavy rains in Sistan and Baluchistan in 2020. The results show that the CYGNSS signal-to-noise ratio observation can be used to detect and map the distribution of a flood disaster, and the results are in good

agreement with the flood disaster distribution obtained from MODIS optical images. Chew et al. [43] proposed a forward model describing changes in the surface reflectance measured by CYGNSS due to floods of different surface types. Both the model and observations indicate that the relationship between surface reflectivity and surface water extent strongly depend on the micro-scale surface roughness of the land and water. Al-Khaldi et al. [44,45] proposed a coherent signal detection method based on the CYGNSS raw count delay-Doppler map (DDM), which marks the coherence by calculating its “diffusion” of the power, and applied the method to inland water-body mapping.

Based on previous studies, this study processed CYGNSS L1 data and used the different sensitivities of surface reflectivity (SR) to different ground features to obtain the range of flooding in Henan Province during one extreme precipitation event. The results showed that using CYGNSS data, one could obtain high spatial resolution flood monitoring results (3, 6 km), and the inversion results revealed the movement of floods between cities over a short period. This further demonstrated the suitability of using satellite-based GNSS-R technology to monitor changes in inland water bodies.

2. Materials and Methods

2.1. Study Area

In mid-July 2021, Typhoon In-fa began to affect eastern and central China. From the Digital Elevation Model (DEM) shown in Figure 1a (DEM data are detailed in Section 2.3), the Taihang Mountains and Funiu Mountains in the northwestern and western part of Henan Province blocked the westward movement of water vapor caused by the typhoon, resulting in abundant water vapor in the central and northern parts of Henan Province, leading to this heavy rainfall. The stable and inactive weather system caused long-term rainfall. Figure 1b shows that among long-term rainfall events, the extremely heavy rainstorm in Zhengzhou on 20 July was the most detrimental, with the maximum rainfall exceeding 600 mm in some areas. However, the rainfall in Zhengzhou rapidly lessened (but was still more than 50 mm) from 21 July onward, and the heavy rainfall shifted northward, affecting the cities of Xinxiang and Hebi in the north of Zhengzhou. Figure 1c,d demonstrate the precipitation distribution on 20 July and 21 July, respectively, in Henan Province derived from the Global Precipitation Measurement (GPM) mission (GPM data are detailed in Section 2.3). Similar to the measured data, the heavy rainfall obviously moved northward on 21 July.

Considering the spatial coverage of CYGNSS data and the characteristics of this heavy rainfall disaster, this study divided the research time into three parts, namely, the stage before the occurrence of heavy rain (1–30 June), the first stage before the heavy rain moved northward (16–20 July), and the second stage after the heavy rain moved northward (21–25 July), to study the distribution characteristics of floods before and after the extreme precipitation moved northward, respectively. As this flood disaster mainly influenced the northern and central parts of Henan Province, Zhengzhou, Xinxiang, Hebi, and Luoyang, which are located in this area, were selected as the main research objects.

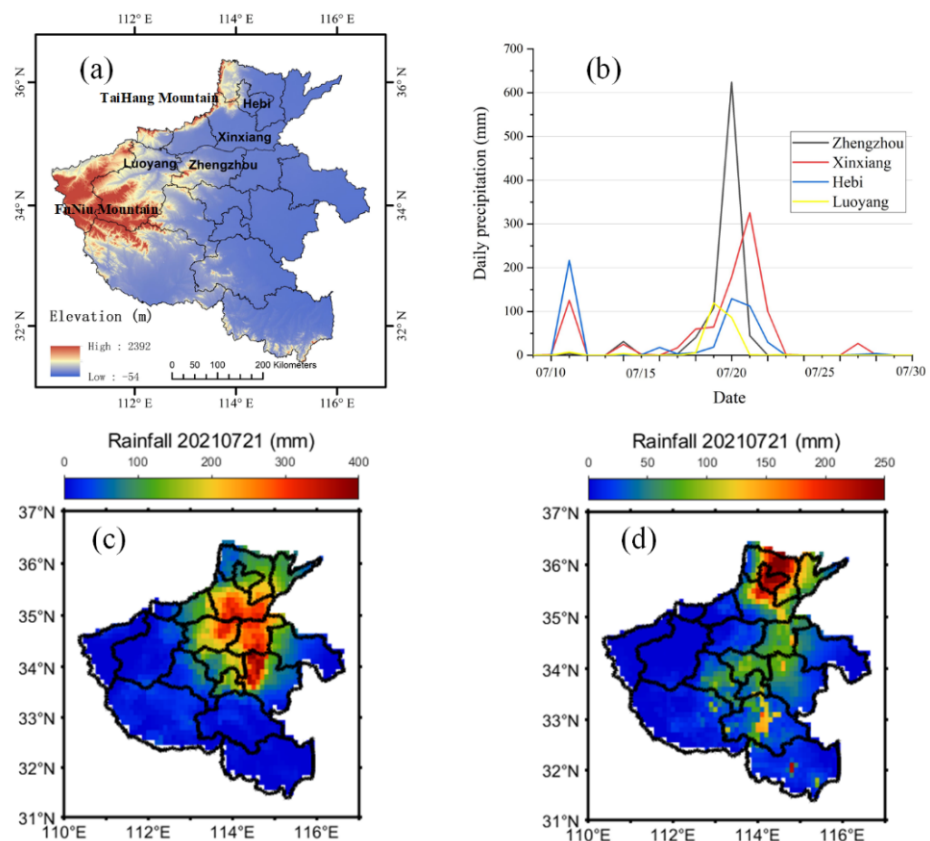


Figure 1. (a) Digital Elevation Model (DEM) in Henan Province; (b) precipitation data measured by some meteorological stations; (c) precipitation in Henan Province on 20 July (Global Precipitation Measurement (GPM)-derived); (d) precipitation in Henan Province on 21 July (GPM-derived).

2.2. CYGNSS Data

The CYGNSS data used in this article is Level 1 Version 3.0, which can be downloaded from <https://podaac.jpl.nasa.gov/> (Accessed date: 12 November 2021). In October 2020, the CYGNSS scientific team released Level 1 Version 3.0 data. Compared with the data included in the previous version (v2.1), this version reevaluates the effective isolated radiated power (EIRP) by using the direct signal power and antenna gain measured by a CYGNSS delay-Doppler measuring instrument, which reduces the uncertainty caused by the antenna pattern [46,47]. In addition, raw intermediate frequency data containing phase information, full DDM data, and software receivers for processing intermediate frequency data have also been released <https://podaac-tools.jpl.nasa.gov/drive/files/allData/cygnss/L1>, accessed on 12 December 2021. Owing to the relative movement of GPS satellites, receivers, the earth, and reflections from different positions around the specular reflection point, a basic observation of the CYGNSS DDM was produced. The CYGNSS Level 1 DDM was composed of 17 delays ($0.25 \mu\text{s}$) \times 11 Doppler (500 Hz). Each CYGNSS Level 1 DDM is formed by 1 ms coherent integration and 1000 ms incoherent accumulation [14,29,46]. Combining the eight small satellites of the CYGNSS mission and the four-channel receiver on each small satellite, CYGNSS can simultaneously provide 32 DDM observations per second. Starting in July 2019, the incoherent integration time of CYGNSS was reduced to 0.5 s. The theoretical terrestrial spatial resolution has also changed from $7 \times 0.5 \text{ km}$ to $3.5 \times 0.5 \text{ km}$. The improvement in spatial resolution is conducive to developing land applications [44]. To ensure the quality of the results, data were filtered according to the following criteria: (1) DDM signal-to-noise ratio (SNR) greater than 1.5 dB; (2) receiver antenna gain greater than 0 dB; and (3) specular reflection point elevation angle greater than 30° .

2.3. Ancillary Data

Due to the lack of real comparison data on spatial and temporal scales, we used a method similar to that reported in a previous study to compare the flooded area derived from CYGNSS [40,41]. The Soil Moisture Active Passive (SMAP) L3 soil moisture product (9×9 km) also works in the L-band to calculate the inundated area. It is a microwave remote sensing satellite that is used for global soil moisture monitoring by NASA and can provide two global soil moisture products, 36×36 km and 9×9 km (9×9 km products are obtained using the Backus–Gilbert interpolation method to process 36×36 km products) [48]. Studies have shown that for unsubmerged land, the upper limit of soil volumetric water content is about $0.4 \text{ cm}^3\text{cm}^{-3}$, and the average water content of submerged land is $0.4\text{--}0.45 \text{ cm}^3\text{cm}^{-3}$ [49]. SMAP data can be downloaded from the NASA National Snow and Ice Data Center website. GPM level 3 10×10 km global rainfall measurement data are obtained from the joint use of a multi-satellite radiometer and an infrared satellite that has been calibrated by microwaves (GPM data can be downloaded from <https://pmm.nasa.gov/>) (Accessed date: 3 October 2021). This study used GPM data to study temporal and spatial changes in precipitation during floods. Concurrently, to evaluate the impact of different land types and land use on the results, remote sensing monitoring data of land use in Henan Province in 2020 was used with a spatial resolution of 1 km. These data were obtained from the Resource and Environmental Science and Data Center of the Chinese Academy of Sciences. The Shuttle Radar Topography Mission 90 m DEM data (v4.1) of the U.S. Space Shuttle Endeavor are used to study the influence of different terrains on flood distribution.

2.4. CYGNSS SR

The working principle of GNSS-R is similar to that of bistatic radar, which involves inverting geophysical parameters by processing L-band signals reflected from the Earth's surface. However, unlike traditional bistatic radar, GNSS-R technology measures the forward scattering signals of navigation satellites and therefore is less susceptible to surface roughness. GNSS-R technology uses a large number of free navigation satellites as signal sources and therefore this technology costs less than other microwave remote sensing technologies. The basic measurement value used in this study is the SR, which is calculated from the DDM observations in the CYGNSS L1 data. Studies have shown that reflectivity largely depends on the physical parameters of the surface, such as soil moisture, surface water, roughness, and vegetation coverage. Generally speaking, for the reflection signals of the L-band navigation satellites used by CYGNSS, a wetter surface will produce a stronger reflectivity, which is the basis of this study.

For a low-orbit satellite in a bistatic configuration, the total power received by the receiver is composed of coherent and incoherent scattering, and its proportion depends on the dielectric constant and roughness of the surface [31]. Therefore, the total bistatic radar scattering power P_{rl} can be determined as follows:

$$P_{rl} = P_{rl}^c + P_{rl}^i \quad (1)$$

Which can be further evaluated as:

$$P_{rl}^c = \frac{P_r^t G^t}{4\pi(R_{ts} + R_{sr})^2} \frac{G^r \lambda^2}{4\pi} \tau_{rl} \quad (2)$$

$$P_{rl}^i = \frac{P_r^t G^t G^r \lambda^2}{(4\pi)^3 R_{ts}^2 R_{sr}^2} \sigma_{rl} \quad (3)$$

where P_{rl}^c and P_{rl}^i are the coherent reflection power and the incoherent scattering power, respectively; P_r^t is the transmit power of the GPS satellite antenna; G^t is the GPS satellite antenna gain; G^r is the CYGNSS antenna gain; R_{ts} and R_{sr} are the distances from the

GPS satellite to the specular point and from the specular point to the CYGNSS receiver, respectively; τ_{rl} represents the SR; and σ_{rl} is the bistatic radar cross-section (m^2).

When using CYGNSS for mapping inland water bodies, we assume that the reflected signal is dominated by coherent reflections [34,37,40] and convert Equation (2) into dB:

$$10 \log P_{rl}^c = 10 \log P_r^t + 10 \log G^t + 10 \log G^r + 20 \log \lambda + 10 \log \tau_{rl} - 20 \log (R_{ts} + R_{sr}) - 20 \log (4\pi) \quad (4)$$

Solving for surface reflectivity, we obtain:

$$\text{SR} = 10 \log \tau_{rl} = 10 \log P_{rl}^c - 10 \log P_r^t - 10 \log G^t - 10 \log G^r - 20 \log \lambda + 20 \log (R_{ts} + R_{sr}) + 20 \log (4\pi) \quad (5)$$

Because DDM is also affected by the incident angle, we added the correction of the incident angle [43]:

$$\text{SR} = \text{SR} - 10 \log \cos^n \theta \quad (6)$$

where θ is the incident angle, n is the correction coefficient, and the value is generally 1.

Notably, the SR calculated using Equations (5) and (6) is negative; in previous studies, a fixed constant was added to the SR to make it positive, which was not done in this study. To further obtain the distribution of flood inundation from the SR, we used the threshold detection method commonly used in CYGNSS inversion of inland surface waters [34,40,41]. The SRs of the permanent water bodies in the studied area were collected, and their average value was taken as the threshold. If a certain SR exceeds this threshold, it can be expected that the SR from inundated areas and non-inundated areas will be lower than the threshold. The detailed process for selecting the threshold is presented in the next section.

For a certain research area, CYGNSS data must be integrated into space and time. Although CYGNSS measurements have a set resolution (over land, the smallest spatial resolution is approximately 3.5 km along-track and 0.5 km across-track, or 5.5 km^2 [50]), owing to the pseudo-random distribution of its observations, for analysis, we need to grid CYGNSS SR to ensure a consistent spatial reference for comparison over time [34]. Considering the three different research stages selected in this study, we used two different grids: 3 × 3 km and 6 × 6 km. The value of each grid depends on the average of all SR measurements falling into the grid.

3. Results

3.1. SR Threshold

To determine the extent of inundation expansion caused by precipitation, we followed the threshold detection method where other monostatic radar data are used to retrieve the inundated area [11,51]. In other words, when the CYGNSS SR exceeds a certain preset threshold, it is considered that the area has been flooded, and vice versa. This method has also been widely used in previous studies using CYGNSS data to retrieve the submerged state of the surface. However, owing to the different parameters, such as the topography, roughness, and vegetation of the studied area, this threshold is not certain [40–42]. For instance, the threshold used by [40] was 12 dB for the medium-vegetation density and typical roughness. However, in another study case with cropland with high soil moisture, high-to-moderate vegetation, and moderate-to-low land cover heterogeneity, the threshold was 17 dB [41]. Therefore, in order to make the results more accurate and reliable, the threshold value should be carefully selected according to the actual situation of the study area.

Figure 2 shows the land cover and land use in Henan Province and the distribution of CYGNSS SR in Henan Province from 1 June to 5 June (scattered form). Different land types such as upland land, paddy fields, forests, and grasslands were widely distributed in Henan Province and the SR was larger when passing through extensive water bodies (paddy fields in the south). The SRs of the different surface features exhibited different characteristics. First, we evaluated the impact of different land types on the CYGNSS SR.

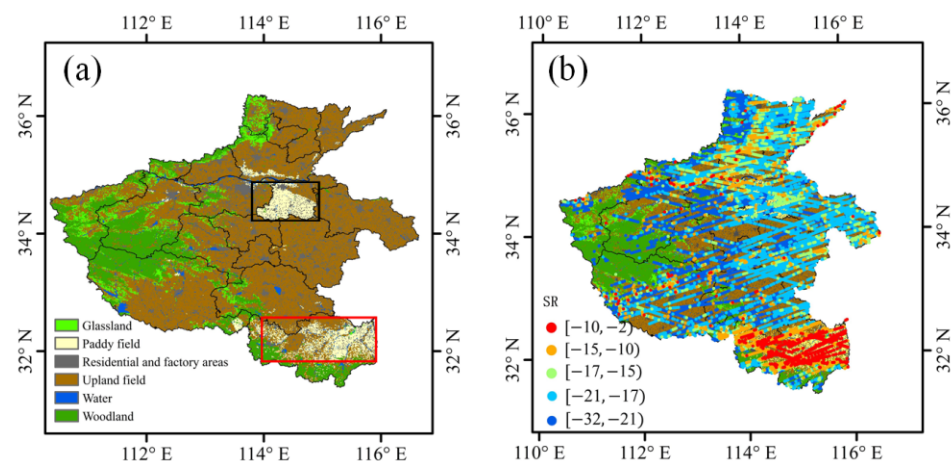


Figure 2. (a) Land use and cover in Henan Province. Note: There are two main rice fields in Henan Province, one in the south (red box) and the other in the north (black box). The planting cycle of the southern rice-producing area is from early May to early September, and the planting cycle of the northern rice-producing area is from mid-July to mid-October. Therefore, during this research period, the rice-producing area in the north was actually planted as upland crops, which can be considered as upland. (b) Cyclone Global Navigation Satellite System (CYGNSS) surface reflectivity (SR) (scattered form) from 1 June to 5 June.

To study differences in SRs corresponding to different land types in Henan Province, we processed all the CYGNSS L1 data (188,815 DDMs) from Henan Province between 1 April and 30 June. The land use and land cover in Henan Province were divided into six types: upland fields, paddy fields, woodlands, grasslands, water, and residential and factory areas. Finally, the spatial analysis method was used to count the number of CYGNSS specular points in different land classes and to compare their corresponding SR and SNR values. Table 1 shows the results of the statistical analyses.

Table 1. Statistical results of surface reflectivity (SR) and signal-to-noise ratio (SNR) of different land types in Henan Province (1 April 2021–30 June 2021).

Land Use and Cover	SR Number	Proportion	SNR (dB)	SR (dB)
Upland field	118,990	63.02%	5.22	−19.13
Paddy field	13,586	7.20%	8.33	−14.58
Woodland	13,589	7.20%	4.53	−21.57
Grassland	7043	3.73%	3.98	−22.49
Water	5388	2.85%	9.16	−13.21
Residential and factory areas	30,219	16.00%	5.56	−18.49

As shown in Table 1, the SR and SNR values corresponding to different land types vary significantly. Although the method used did not consider the influence of terrain and surface roughness, statistical results still indicated differential sensitivity of CYGNSS data to different features. For example, water and paddy fields had the highest SR values of approximately −13 dB and −15 dB, respectively; woodland and grassland had the lowest SR values of approximately −22 dB; and upland field and residential and factory areas had similar SR values of approximately −19 dB. The statistical results of the SNR values were similar to those of the SR values, with the highest values found for water and paddy fields, approximately 9 dB and 8 dB, respectively; followed by upland field and residential and factory areas at approximately 5 dB; and the lowest values found for woodland and grassland areas, at approximately 4 dB. Further in-depth research requires higher-resolution land use and land cover data, and simultaneously, a more refined classification of ground features is required. For example, forest land can be further classified into forests and low shrubs. Finally, the influence of the surface roughness around the specular reflection point

must also be considered. Based on the statistical results in Table 1, we used -13 dB as the SR threshold for this study.

3.2. DDM Changes before and after Flooding

The basic observation information provided by CYGNSS is the DDM. The DDM reflected by the land mainly depends on the dielectric constant, roughness, and vegetation coverage near the specular point (which, for smooth reflecting surfaces, is approximately the size of the first Fresnel zone). Generally, in the case of medium-to-low vegetation coverage, the flatter the reflecting surface, the stronger the energy of the reflected signal and the more concentrated the reflected power received in the DDM. For a rough surface, scattering near the specular point will make the generated DDM appear as typical or atypical horseshoe shapes [45]. Therefore, after the flood, the corresponding DDM will change with variations in the reflective surface properties of flooded areas.

Figure 3 shows changes in the DDM before and after floods in the same area. On 5 June, before the flood occurred, the DDM showed a clear horseshoe shape, and the power distribution was relatively scattered. On 23 July, the area was submerged by water, the DDM showed obvious changes, the reflected signal energy increased, and the power was mainly concentrated in a few pixels. On 13 August, the flood subsided, and the power distribution in the DDM reappeared in the shape of a horseshoe, similar to before the flood. Table 2 shows the detailed information of these three DDMs.

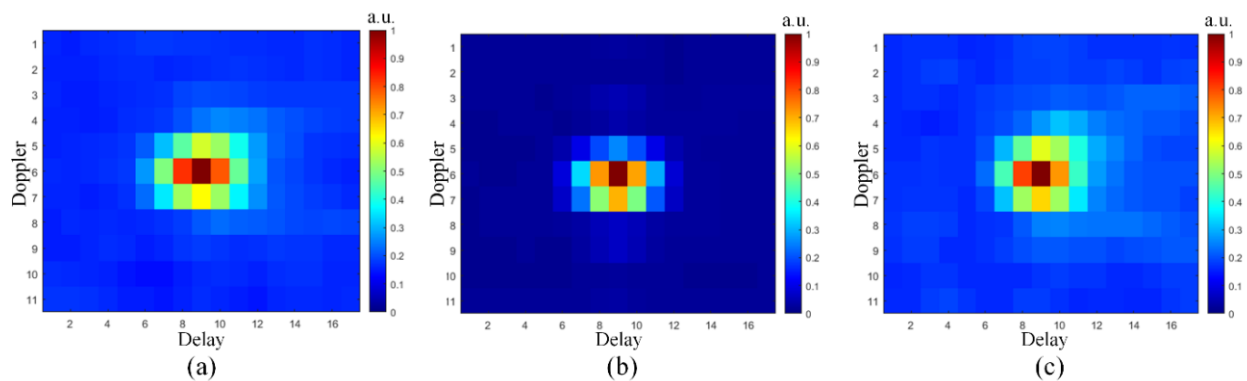


Figure 3. Delay-Doppler map (DDM) changes before and after floods in the same area. (a) 5 June (before the flood); (b) 23 July (flooding); (c) 13 August (after the flood).

Table 2. Changes in delay-Doppler map (DDM) parameters before and after floods in the same area. Effective isolated radiated power (EIRP), surface reflectivity (SR), and signal-to-noise ratio (SNR).

Date	Satellite Number	SP Position		Track Number	EIRP (Watt)	SNR (dB)	SR (dB)
5 June	Cy02	114°19' E	34°42' N	251	528.57	8.03	-17.96
23 July	Cy03	114°15' E	34°48' N	466	724.74	16.93	-6.15
13 August	Cy02	114°16' E	34°42' N	969	595.33	7.67	-18.25

Table 2 provides more detailed statistics on the parameter information of the three DDMs in Figure 3. After the flood occurred, the SNR and SR in the same area increased significantly by 9 dB and 12 dB, respectively. When the flood subsided, the SNR and SR dropped to pre-flood levels. Changes in the DDM parameters in Table 2 confirm the effectiveness of using the SR threshold method to monitor flood distribution.

3.3. SMAP Flood-Monitoring Results

For comparison with the CYGNSS results, we also used SMAP data to invert the submerged area because the working frequency bands of SMAP and CYGNSS are both in the L-band, and their sensitivity to surface physical parameters is similar. As mentioned

in the Materials and Methods section, we believe that when the soil moisture is greater than $0.4 \text{ cm}^3 \text{ cm}^{-3}$, the area is covered by water, and vice versa. Figure 4 shows the change in SMAP soil moisture before and after the flood as well as the flood distribution range obtained by the threshold method.

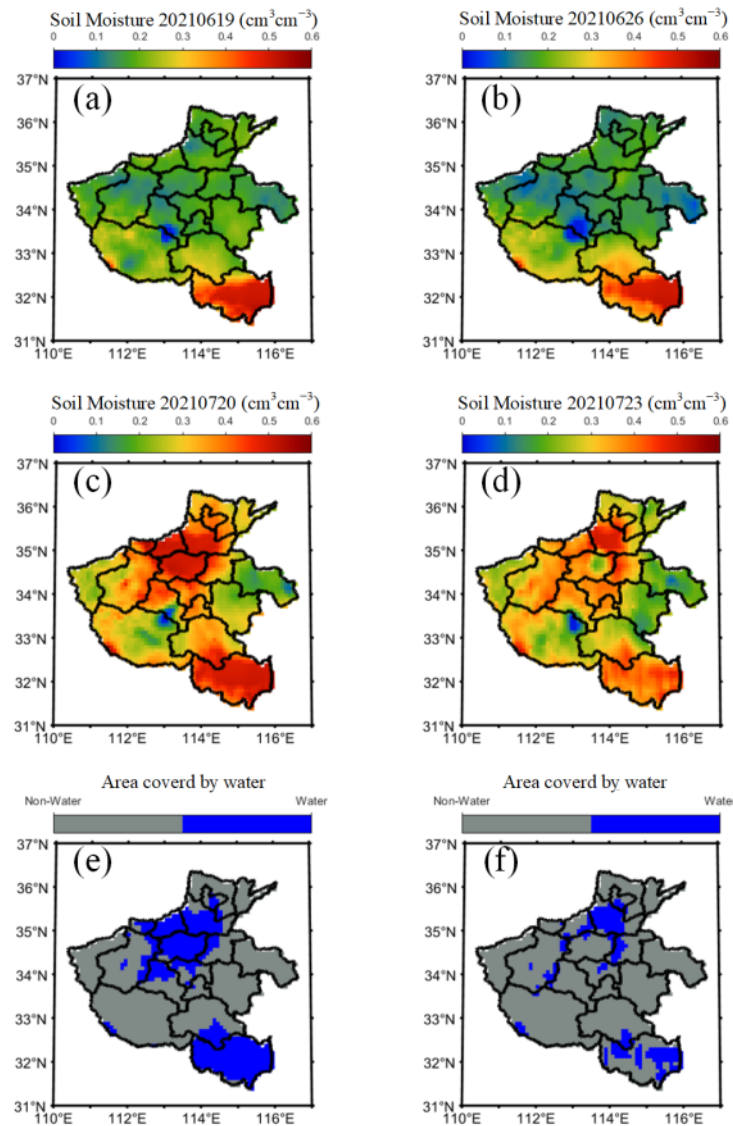


Figure 4. Soil Moisture Active Passive (SMAP) soil moisture changes before and after floods in Henan Province and the results of SMAP inversion of flood areas. (a) SMAP soil moisture on 19 June; (b) SMAP soil moisture on 26 June; (c) SMAP soil moisture on 20 July; (d) SMAP soil moisture on 23 July; (e) SMAP inversion results of floods in the first stage of heavy rainfall (16–20 July); (f) SMAP inversion results of floods in the second stage of heavy rainfall (21–25 July).

Figure 4 highlights that before the floods (Figure 4a,b), most areas of Henan Province, except for the rice-producing areas in the south, had soil moisture between $0.05\text{--}0.3 \text{ cm}^3 \text{ cm}^{-3}$. After the heavy rain triggered floods in mid-July, the soil moisture values in the northern and central parts of Henan Province increased rapidly (Figure 4c,d) and exceeded $0.45 \text{ cm}^3 \text{ cm}^{-3}$ in some areas. Figure 4e shows that during the first stage of heavy rainfall, large areas of central and northern Henan were flooded. However, due to the limited resolution of the SMAP satellite ($36 \times 36 \text{ km}$), the results of the inversion revealed a large-flooded-area effect, which was clearly not in line with observed events. Figure 4f demonstrates the results of the SMAP satellite during the second stage of heavy rainfall. Flood disasters moved northward, but the results revealed that Zhengzhou was not

submerged at this stage, which was unrealistic. It should be noted that Figure 4e,f both show the characteristics of land inundation in the rice-producing areas in southern Henan Province and denote the Danjiangkou Reservoir in southwestern Henan Province.

3.4. CYGNSS Flood-Monitoring Results

The four cities most severely affected by this flood are Zhengzhou, Luoyang, Xinxiang, and Hebi. In this section, we present the distribution of submerged areas corresponding to different rainfall stages obtained using the CYGNSS data. First, we studied the changes in the CYGNSS SR in Henan Province before and after the occurrence of heavy rainfall.

Figure 5a–c show the gridded CYGNSS SR at three different stages. Considering the different time spans of the three stages, we used 6×6 km and 3×3 km grids. The water-covered areas (southern Henan Province) and the central and northern parts of Henan Province after heavy rainfall have larger corresponding SRs (Figure 5b,c). Notably, because the spatial resolution is better than SMAP, the CYGNSS results shown in Figure 5 are finer than those shown in Figure 4. For example, the CYGNSS results show the contrast between the submerged and unsubmerged areas in central Henan Province when the flood occurred (Figure 4d,e). Furthermore, the threshold method was used to analyze the results.

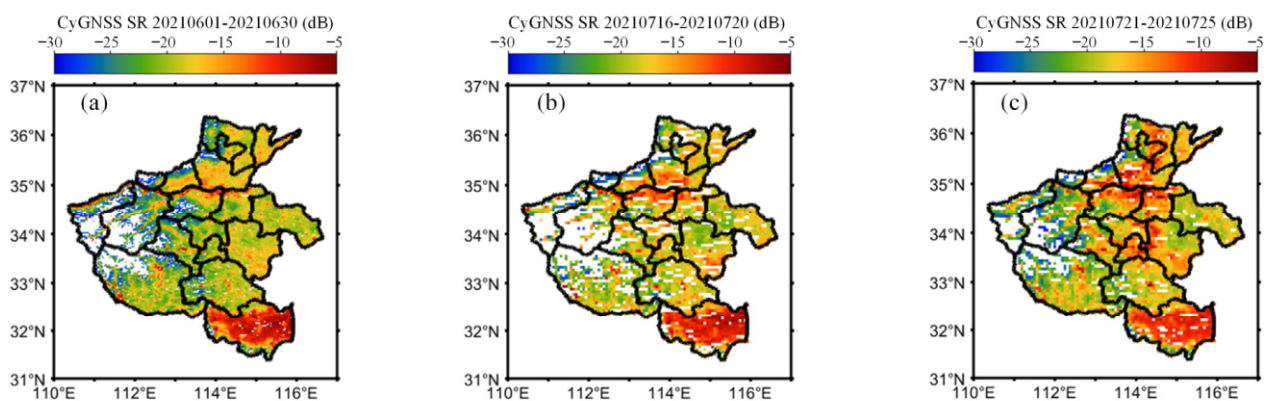


Figure 5. Gridded Cyclone Global Navigation Satellite System surface reflectivity (CYGNSS SR) before and after extreme precipitation in Henan Province. (a) Gridded SR before the occurrence of heavy rainfall (3×3 km); (b) Gridded SR in the first stage of heavy rainfall (6×6 km); (c) Gridded SR in the second stage of heavy rainfall (6×6 km).

According to the results in Section 3.1, we used -13 dB as the threshold to distinguish inundated areas from non-inundated areas. Any grid with a value greater than -13 dB will be marked as inundated. It should be noted that although we used -13 dB as the threshold, the highest non-erroneous SR value after data preprocessing is about -5 dB. Figure 6a–c highlight the three different stages of surface water coverage in Henan Province when the threshold is -13 dB. As shown in Figure 6a, in the stage before the occurrence of extreme precipitation, only the southern rice-producing areas of Henan Province showed a large-scale flooded state, and the CYGNSS data accurately detected the existence of inland water bodies. Notably, (1) the CYGNSS data accurately detected the Yellow River in Henan Province (the river width is about 500–600 m) and accurately mapped the complete spatial shape of the Yellow River in the study area, and (2) the Danjiangkou Reservoir in southwestern Henan Province was also accurately detected. The successful inversion of rivers and reservoirs further demonstrates the ability to use CYGNSS data to detect smaller inland water bodies.

Figure 6b shows the distribution of floods caused by the first stage of heavy rainfall in Henan Province. Zhengzhou was mostly submerged, Xinxiang was partially submerged, and Hebi and Luoyang were not submerged, as shown in the figure. The flood distribution obtained from the CYGNSS data was consistent with the actual situation of the first stage of extreme precipitation, which mainly affected Zhengzhou in central Henan Province,

thus flooding most of the area. At this time, the water vapor brought by the typhoon did not move northward.

Figure 6c shows the area flooded during the second stage of the extreme precipitation. After 20 July, a large amount of water vapor moved northward, and heavy rainfall began to affect Xinxiang and Hebi in northern Henan Province. The regional distribution of floods obtained from CYGNSS also confirmed this point. As shown in Figure 6c, at this stage, Zhengzhou was partially flooded, Xinxiang was mostly flooded, Hebi was partially flooded, and Luoyang was not flooded. The distribution of floods is consistent with the actual situation.

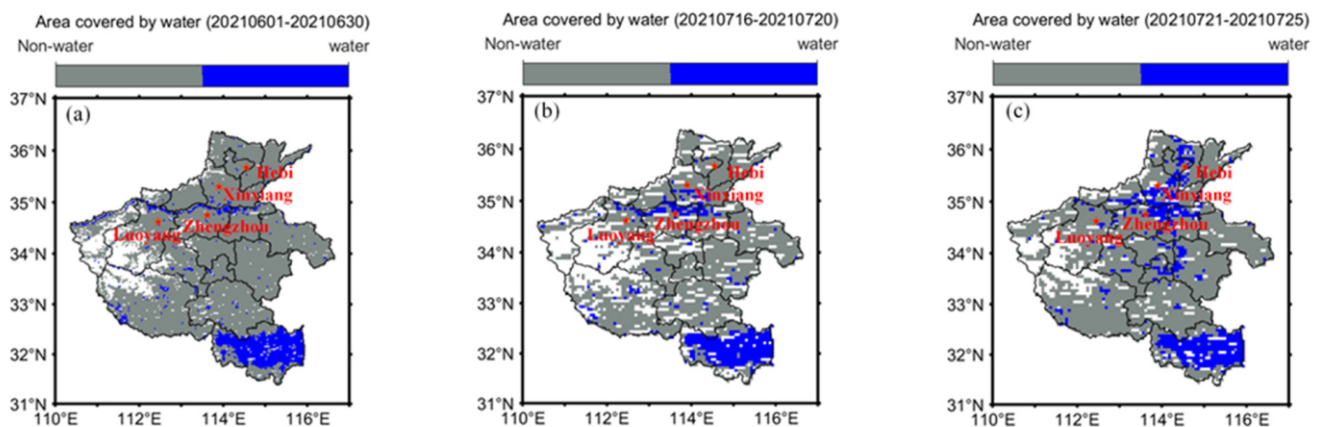


Figure 6. The distribution map of surface inundation before and after heavy rainfall in Henan Province obtained by Cyclone Global Navigation Satellite System surface reflectivity (CYGNSS SR). (a) Distribution of surface inundation before the occurrence of extreme precipitation (1 June 2021–30 June 2021); (b) Distribution of floods in the first stage of extreme precipitation (16 July 2021–20 July 2021); (c) Flood distribution in the second stage of extreme precipitation (21 July 2021–25 July 2021). The red pentagram represents the locations of Zhengzhou, Xinxiang, Hebi, and Luoyang. The corresponding relationship is shown in Figure 1.

The results obtained from the CYGNSS data indicate the movement of floods from city to city over a relatively short period of time. Notably, Luoyang is located in the western part of Henan Province with high terrain, and the high mountain system between Zhengzhou and Luoyang hinders the water vapor from moving westward to a certain extent, so most areas of Luoyang were not affected by the flood disaster during this extreme precipitation event. Figure 6b,c also show that Luoyang is not submerged, which is consistent with observations.

3.5. Time Series Analysis

The previous section details spatial changes before and during the flood. This section mainly discusses temporal changes in rainfall, soil moisture, and the SR. Figure 7 shows changes in the daily precipitation, daily soil moisture, and daily SR around 34° N and 114° E from 1 June to 31 August. This area is located in the southwest of Zhengzhou, with an altitude of approximately 100 m. The terrain is low and dominated by flat farmlands. Heavy rainfall can easily cause floods in this area.

As shown in Figure 7, before 20 July, the soil moisture was below $0.3 \text{ cm}^3 \text{ cm}^{-3}$, and although the SR fluctuated with the change of precipitation, it was below -17 dB . On 20 July, Zhengzhou was hit by torrential rain, the soil moisture increased to $0.5 \text{ cm}^3 \text{ cm}^{-3}$, and, correspondingly, the SR increased sharply, which indicated that the area was flooded at this time. After 20 July, the flood gradually dissipated, and the soil moisture and SR slowly decreased over time to below $0.4 \text{ cm}^3 \text{ cm}^{-3}$ and -16 dB , respectively. In August, the soil moisture and SR fluctuated greatly, which may have been caused by repeated rainfall in the area. In general, the time evolution of SR is similar to the time evolution of

soil moisture ($r = 0.7$), which demonstrates that changes in SR indicate changes in surface inundation.

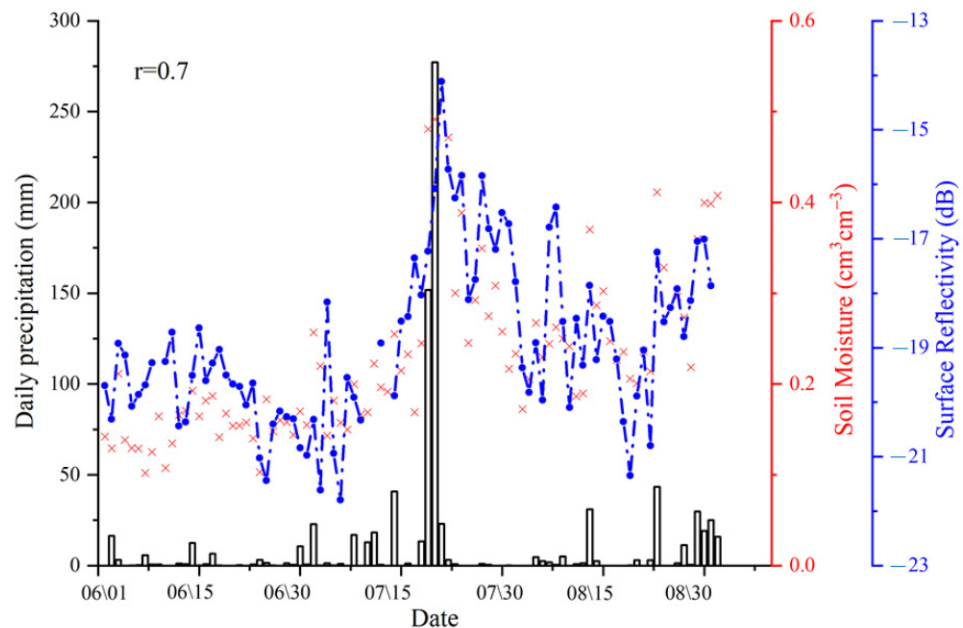


Figure 7. Changes in precipitation, soil moisture, and reflectivity near (34° N, 114° E) from 1 June to 31 August 2021. Rainfall (black bar graph), soil moisture (red scatter graph), and surface reflectivity (SR) (blue dotted line graph). $r = 0.7$.

4. Discussion

Sections 3.4 and 3.5 discuss the feasibility of using CYGNSS SR to monitor flood distribution. It not only successfully captured the spatial and temporal trends before and after submergence, but also detected the changes in the areas affected by the floods over a relatively short period. Compared with other methods using remote sensing satellites to monitor floods, this method did not require input on the influences of uncertain factors such as cloud cover and satellite revisit time, and the resolution of the results was higher. This is a simple and effective flood-monitoring method. In fact, in addition to being used for flood monitoring, CYGNSS technology has also shown great potential in monitoring global climate change in recent years. For example, CYGNSS has been used for monitoring wetland area change [52], coastal flooding [53], and sea level rise [54]. These applications can help researchers better understand the framework of climate change, and can also be used as a reference when relevant departments formulate corresponding climate policies [55]. However, it should be noted that although the results shown in Figure 6 successfully proved the feasibility of using CYGNSS data to obtain a higher spatial resolution of flood distribution, the temporal resolution was still limited to five days. This is due to the pseudo-random distribution of CYGNSS specular reflection points, and the fact that sufficient SR observations must be accumulated into a specific grid. Therefore, a finer spatial grid is inherently associated with a coarser temporal resolution. To plot the flood distribution more frequently (for example, every day), a coarser spatial grid (for example, 25 km or larger) is required. In addition, this method has several limitations: (1) when determining whether the ground surface is covered by water, the simple threshold method must be studied further; (2) CYGNSS uses the DTU10 (Technical University of Denmark 10) global sea surface model, which does not consider the impact of land terrain, resulting in large errors in the estimation of land specular reflection points at altitudes greater than 600 m, which creates flood detection problems in some areas with higher altitudes; (3) like other microwave remote sensing data, CYGNSS data is also affected by

terrain, vegetation coverage, and roughness. To obtain more accurate flood distribution data, additional corrections must be added to the algorithm.

5. Conclusions

Flood monitoring not only plays an important role in disaster prevention and mitigation, but also has great practical significance for understanding the temporal and spatial evolution of floods, forecasting floods, and creating flood early-warning systems. Based on the sensitivity of CYGNSS data to surface water, this study proposed a signal scattering mechanism and analyzed temporal and spatial changes of SR before and after extreme precipitation in Henan Province. The distribution of flood disasters in different stages of heavy rainfall was obtained and compared with the SMAP method. The results showed that compared to the detection results of SMAP, the flood distributions obtained by the two methods were similar, but those obtained by CYGNSS had a higher resolution and could monitor the changes of the areas affected by the floods over a shorter period. Although the CYGNSS mission was originally designed to monitor the tropical sea surface wind field, in recent years, many land-surface remote sensing studies have shown the CYGNSS mission's sensitivity to soil moisture, wetlands, and floods. Its monitoring capability is equivalent to that of current common bistatic radar. The short revisit time also demonstrates that CYGNSS is suitable for highly dynamic flood monitoring. With the launch of more GNSS-R satellites focusing on terrestrial applications in the future [56], there will be more high-quality and high-temporal-resolution space-borne GNSS-R data, which will undoubtedly further promote the development of GNSS-R land-surface and coastal-monitoring remote sensing.

Author Contributions: Conceptualization, S.Z., Z.M. and Z.L.; methodology, S.Z., Z.M., Q.L. and Y.N.; software, Z.M.; validation, Z.M., J.Z., S.H., Y.F. and H.Z.; writing—original draft preparation, Z.M. and S.Z.; writing—review and editing, Z.L. and P.Z.; supervision, Z.L. All authors have read and agreed to the published version of the manuscript.

Funding: This research was funded by the National Natural Science Foundation of China Projects (42074041,41731066); The National Key Research and Development Program of China (2020YFC1512000, 2019YFC1509802); State Key Laboratory of Geo-Information Engineering (SKLGIE2019-Z-2-1); Shaanxi Natural Science Research Program (2020JM-227).

Institutional Review Board Statement: Not applicable.

Informed Consent Statement: Not applicable.

Data Availability Statement: Not applicable.

Acknowledgments: The author would like to thank NASA for providing CYGNSS, SMAP, GPM, and SRTM DEM data. Thanks to the Resource and Environmental Science and Data Center of the Chinese Academy of Sciences for the land use and classification data. Thanks to the China Meteorological Administration for providing the measured rainfall data. All anonymous reviewers and editors are thanked for their constructive review of this manuscript.

Conflicts of Interest: The authors declare no conflict of interest.

References

1. Available online: http://www.gov.cn/guoqing/2018-01/17/content_5257444.htm (accessed on 2 November 2021).
2. Available online: http://www.cma.gov.cn/2011wmhd/2011wzbf/2011wftzb/202107/t20210720_581150.html (accessed on 2 November 2021).
3. Available online: http://www.cma.gov.cn/2011xwzx/2011xgzdt/202107/t20210721_581188.html (accessed on 2 November 2021).
4. Jonkman, S.N. Global perspectives on loss of human life caused by floods. *Nat. Hazards* **2005**, *34*, 151–175. [[CrossRef](#)]
5. Hirabayashi, Y.; Mahendran, R.; Koirala, S.; Konoshima, L.; Yamazaki, D.; Watanabe, S.; Kim, H.; Kanae, S. Global flood risk under climate change. *Nat. Clim. Chang.* **2013**, *3*, 816–821. [[CrossRef](#)]
6. Klemas, V. Remote sensing of floods and flood-prone areas: An overview. *J. Coast. Res.* **2015**, *31*, 1005–1013. [[CrossRef](#)]
7. Bates, P.D. Remote sensing and flood inundation modelling. *Hydrol. Process.* **2004**, *18*, 2593–2597. [[CrossRef](#)]
8. Asner, G.P. Cloud cover in Landsat observations of the Brazilian Amazon. *Int. J. Remote Sens.* **2001**, *22*, 3855–3862. [[CrossRef](#)]

9. Rundquist, D.C.; Narumalani, S.; Narayanan, R.M. A review of wetlands remote sensing and defining new considerations. *Remote Sens. Rev.* **2001**, *20*, 207–226. [[CrossRef](#)]
10. Klemas, V.; Pieterse, A. *Advances in Watershed Science and Assessment. The Handbook of Environmental Chemistry*; Springer: Berlin/Heidelberg, Germany, 2015; Volume 33.
11. Kuenzer, C.; Guo, H.; Huth, J.; Leinenkugel, P.; Li, X.; Dech, S. Flood mapping and flood dynamics of the Mekong Delta: ENVISAT-ASAR-WSM based time series analyses. *Remote Sens.* **2013**, *5*, 687–715. [[CrossRef](#)]
12. Hall, C.; Cordey, R. Multistatic scatterometry. In Proceedings of the IEEE International Geoscience Remote Sensing Symposium, Edinburgh, UK, 12–16 September 1988; pp. 561–562.
13. Martin-Neira, M. A Passive Reflectometry and Interferometry System (PARIS): Application to ocean altimetry. *ESA J.* **1993**, *17*, 331–355.
14. Zavorotny, V.U.; Voronovich, A.G. Scattering of GPS signals from the ocean with wind remote sensing application. *IEEE Trans. Geosci. Remote Sens.* **2000**, *38*, 951–964. [[CrossRef](#)]
15. Yu, K.; Wang, S.; Li, Y.; Chang, X. Snow depth estimation with GNSS-R dual receiver observation. *Remote Sens.* **2019**, *11*, 2056. [[CrossRef](#)]
16. Wu, X.R.; Jin, S.G. Models and theoretical analysis of SoOP circular polarization bistatic scattering for random rough surfaces. *Remote Sens.* **2020**, *12*, 1506. [[CrossRef](#)]
17. Tabibi, S.; Francis, O. Can GNSS-R Detect Abrupt Water Level Changes? *Remote Sens.* **2020**, *12*, 3614. [[CrossRef](#)]
18. Pan, Y.; Ren, C.; Liang, Y.; Zhang, Z.; Shi, Y. Inversion of surface vegetation water content based on GNSS-IR and MODIS data fusion. *Satell. Navig.* **2020**, *1*, 21. [[CrossRef](#)]
19. Zhang, S.; Wang, T.; Wang, L.; Zhang, J.; Peng, J.; Liu, Q. Evaluation of GNSS-IR for Retrieving Soil Moisture and Vegetation Growth Characteristics in Wheat Farmland. *J. Surv. Eng.* **2021**, *147*, 04021009. [[CrossRef](#)]
20. Gao, F.; Xu, T.; Meng, X.; Wang, N.; He, Y.; Ning, B. A Coastal Experiment for GNSS-R Code-Level Altimetry Using BDS-3 New Civil Signals. *Remote Sens.* **2021**, *13*, 1378. [[CrossRef](#)]
21. Lowe, S.T.; Labrecque, J.L.; Zuffada, C.; Romans, L.J.; Young, L.E.; Hajj, G.A. First spaceborne observation of an Earth-reflected GPS signal. *Radio Sci.* **2002**, *37*, 7. [[CrossRef](#)]
22. Gleason, S.; Hodgart, S.; Sun, Y.; Gommenginger, C.; Mackin, S.; Adjrard, M.; Unwin, M. Detection and Processing of bistatically reflected GPS signals from low Earth orbit for the purpose of ocean remote sensing. *IEEE Trans. Geosci. Remote Sens.* **2005**, *43*, 1229–1241. [[CrossRef](#)]
23. Unwin, M.; Jales, P.; Blunt, P.; Duncan, S. Preparation for the First Flight of SSTL's Next Generation Space GNSS Receivers. In Proceedings of the 6th ESA/European Workshop Satellite NAVITEC GNSS Signals Signal Processor, Noordwijk, The Netherlands, 5–7 December 2012; pp. 1–6.
24. Ruf, C.; Unwin, M.; Dickinson, J.; Rose, R.; Rose, D.; Vincent, M.; Lyons, A. CYGNSS: Enabling the Future of Hurricane Prediction [Remote Sensing Satellites]. *IEEE Geosci. Remote Sens. Mag.* **2013**, *1*, 52–67. [[CrossRef](#)]
25. Ruf, C.; Atlas, R.; Chang, P.S.; Clarizia, M.P.; Garrison, J.L.; Gleason, S.; Katzberg, S.J.; Jelenak, Z.; Johnson, J.T.; Majumdar, S.J.; et al. New Ocean Winds Satellite Mission to Probe Hurricanes and Tropical Convection. *Bull. Am. Meteorol. Soc.* **2015**, *97*, 385–395. [[CrossRef](#)]
26. Ruf, C.; Chang, P.S.; Clarizia, M.P.; Gleason, S.; Jelenak, Z.; Majumdar, S.; Morris, M.; Murray, J.; Musko, S.; Posselt, D.; et al. *CYGNSS Handbook. Cyclone Global Navigation Satellite System*; Michigan Publishing: Ann Arbor, MI, USA, 2016.
27. Bu, J.; Yu, K.; Zhu, Y.; Qian, N.; Chang, J. Developing and Testing Models for Sea Surface Wind Speed Estimation with GNSS-R Delay Doppler Maps and Delay Waveforms. *Remote Sens.* **2020**, *12*, 3760. [[CrossRef](#)]
28. Li, X.; Yang, D.; Wang, J.; Zheng, G.; Han, G.; Nan, Y.; Li, W. Analysis of coastal wind speed retrieval from CYGNSS mission using artificial neural network. *Remote Sens. Environ.* **2021**, *260*, 112454. [[CrossRef](#)]
29. Camps, A.; Park, H.; Pablos, M.; Foti, G.; Gommenginger, C.P.; Liu, P.W.; Judge, J. Sensitivity of GNSS-R Spaceborne Observations to Soil Moisture and Vegetation. *IEEE J. Sel. Top. Appl. Earth Obs. Remote Sens.* **2016**, *9*, 4730–4742. [[CrossRef](#)]
30. Chew, C.C.; Small, E.E. Soil Moisture Sensing Using Spaceborne GNSS Reflections: Comparison of CYGNSS Reflectivity to SMAP Soil Moisture. *Geophys. Res. Lett.* **2018**, *45*, 4049–4057. [[CrossRef](#)]
31. Kim, H.; Lakshmi, V. Use of Cyclone Global Navigation Satellite System (CyGNSS) Observations for Estimation of Soil Moisture. *Geophys. Res. Lett.* **2018**, *45*, 8272–8282. [[CrossRef](#)]
32. Yan, Q.; Huang, W.; Jin, S.; Jia, Y. Pan-tropical soil moisture mapping based on a three-layer model from CYGNSS GNSS-R data. *Remote Sens. Environ.* **2020**, *247*, 111944. [[CrossRef](#)]
33. Santi, E.; Paloscia, S.; Pettinato, S.; Fontanelli, G.; Clarizia, M.P.; Comite, D.; Dente, L.; Guerriero, L.; Pierdicca, N.; Floury, N. Remote Sensing of Forest Biomass Using GNSS Reflectometry. *IEEE J. Sel. Top. Appl. Earth Obs. Remote Sens.* **2020**, *13*, 2351–2368. [[CrossRef](#)]
34. Morris, M.; Chew, C.; Reager, J.T.; Shah, R.; Zuffada, C. A novel approach to monitoring wetland dynamics using CYGNSS: Everglades case study. *Remote Sens. Environ.* **2019**, *233*, 111417. [[CrossRef](#)]
35. Carrenoluengo, H.; Luzi, G.; Crosetto, M. Above-Ground Biomass Retrieval over Tropical Forests: A Novel GNSS-R Approach with CyGNSS. *Remote Sens.* **2020**, *12*, 1368. [[CrossRef](#)]
36. Li, W.; Cardellach, E.; Fabra, F.; Ribó, S.; Rius, A. Lake Level and Surface Topography Measured With Spaceborne GNSS-Reflectometry from CYGNSS Mission: Example for the Lake Qinghai. *Geophys. Res. Lett.* **2018**, *45*, 13–332. [[CrossRef](#)]

37. Gerlein-Safdi, C.; Ruf, C.S. A CYGNSS-based algorithm for the detection of inland waterbodies. *Geophys. Res. Lett.* **2019**, *46*, 12065–12072. [[CrossRef](#)]
38. Ruf, C.; Chew, C.; Gerlein-Safdi, C.; Warnock, A. Resolving Inland Waterways with CYGNSS. In Proceedings of the 2021 IEEE International Geoscience and Remote Sensing Symposium IGARSS, Brussels, Belgium, 11–16 July 2021; pp. 954–957.
39. Cheong, J.W.; Southwell, B.J.; Dempster, A.G. Blind Sea Clutter Suppression for Spaceborne GNSS-R Target Detection. *IEEE J. Sel. Top. Appl. Earth Obs. Remote Sens.* **2019**, *12*, 5373–5378. [[CrossRef](#)]
40. Chew, C.; Reager, J.T.; Small, E. CYGNSS data map flood inundation during the 2017 Atlantic hurricane season. *Sci. Rep.* **2018**, *8*, 9336. [[CrossRef](#)]
41. Wan, W.; Liu, B.; Zeng, Z.; Chen, X.; Wu, G.; Xu, L.; Chen, X.; Hong, Y. Using CYGNSS Data to Monitor China's Flood Inundation during Typhoon and Extreme Precipitation Events in 2017. *Remote Sens.* **2019**, *11*, 854. [[CrossRef](#)]
42. Rajabi, M.; Nahavandchi, H.; Hoseini, M. Evaluation of CYGNSS Observations for Flood Detection and Mapping during Sistan and Baluchestan Torrential Rain in 2020. *Water* **2020**, *12*, 2047. [[CrossRef](#)]
43. Chew, C.; Small, E. Estimating inundation extent using CYGNSS data: A conceptual modeling study. *Remote Sens. Environ.* **2020**, *246*, 111869. [[CrossRef](#)]
44. Al-Khaldi, M.M.; Johnson, J.T.; Gleason, S.; Loria, E.; O'Brien, A.J.; Yi, Y. An Algorithm for Detecting Coherence in Cyclone Global Navigation Satellite System Mission Level-1 Delay-Doppler Maps. *IEEE Trans. Geosci. Remote Sens.* **2020**, *59*, 4454–4463. [[CrossRef](#)]
45. Al-Khaldi, M.M.; Johnson, J.T.; Gleason, S.; Chew, C.C.; Gerlein-Safdi, C.; Shah, R.; Zuffada, C. Inland Water Body Mapping Using CYGNSS Coherence Detection. *IEEE Trans. Geosci. Remote Sens.* **2021**, *59*, 7385–7394. [[CrossRef](#)]
46. Gleason, S.; Ruf, C.S.; O'Brien, A.J.; McKague, D.S. The CYGNSS Level 1 Calibration Algorithm and Error Analysis Based on On-Orbit Measurements. *IEEE J. Sel. Top. Appl. Earth Obs. Remote Sens.* **2018**, *12*, 37–49. [[CrossRef](#)]
47. Ruf, C.; Asharaf, S.; Balasubramaniam, R.; Gleason, S.; Lang, T.; McKague, D.; Twigg, D.; Waliser, D. In-Orbit Performance of the Constellation of CYGNSS Hurricane Satellites. *Bull. Am. Meteorol. Soc.* **2019**, *100*, 2009–2023. [[CrossRef](#)]
48. Chaubell, J.; Yueh, S.; Entekhabi, D.; Peng, J. Resolution enhancement of SMAP radiometer data using the Backus Gilbert optimum interpolation technique. In Proceedings of the 2016 IEEE International Geoscience and Remote Sensing Symposium (IGARSS), Beijing, China, 11–15 July 2016; pp. 284–287.
49. Rahman, M.S.; Di, L.; Shrestha, R.; Yu, E.G.; Lin, L.; Zhang, C.; Hu, L.; Tang, J.; Yang, Z. Agriculture flood mapping with Soil Moisture Active Passive (SMAP) data: A case of 2016 Louisiana flood. In Proceedings of the 2017 6th International Conference on Agro-Geoinformatics, Fairfax, VA, USA, 7–10 August 2017; pp. 1–6.
50. Chew, C. Spatial interpolation based on previously-observed behavior: A framework for interpolating spaceborne GNSS-R data from CYGNSS. *J. Spat. Sci.* **2021**, 1–14. [[CrossRef](#)]
51. Kiage, L.M.; Walker, N.D.; Balasubramanian, S.; Babin, A.; Barras, J. Applications of Radarsat-1 synthetic aperture radar imagery to assess hurricane-related flooding of coastal Louisiana. *Int. J. Remote Sens.* **2005**, *26*, 5359–5380. [[CrossRef](#)]
52. Gerlein-Safdi, C.; Bloom, A.A.; Plant, G.; Kort, E.A.; Ruf, C.S. Improving representation of tropical wetland methane emissions with CYGNSS inundation maps. *Earth Space Sci. Open Arch. ESSOAr* **2020**. [[CrossRef](#)]
53. Scicchitano, G.; Scardino, G.; Monaco, C.; Piscitelli, A.; Milella, M.; De Giosa, F.; Mastronuzzi, G. Comparing impact effects of common storms and Medicanes along the coast of south-eastern Sicily. *Mar. Geol.* **2021**, *439*, 106556. [[CrossRef](#)]
54. Anzidei, M.; Scicchitano, G.; Scardino, G.; Bignami, C.; Tolomei, C.; Vecchio, A.; Serpelloni, E.; De Santis, V.; Monaco, C.; Milella, M.; et al. Relative Sea-Level Rise Scenario for 2100 along the Coast of South Eastern Sicily (Italy) by InSAR Data, Satellite Images and High-Resolution Topography. *Remote Sens.* **2021**, *13*, 1108. [[CrossRef](#)]
55. Available online: <https://www.ipcc.ch/> (accessed on 13 December 2021).
56. Carreno-Luengo, H.; Crespo, J.A.; Akbar, R.; Morris, M.; Ruf, C. The CYGNSS Mission: On-Going Science Team Investigations. *Remote Sens.* **2021**, *13*, 1814. [[CrossRef](#)]